

# In-N-Out: Face Video Inversion and Editing with Volumetric Decomposition

Yiran Xu<sup>1</sup> Zhixin Shu<sup>2</sup> Cameron Smith<sup>2</sup> Jia-Bin Huang<sup>1</sup> Seoung Wug Oh<sup>2</sup>

<sup>1</sup>University of Maryland, College Park, <sup>2</sup>Adobe Research

<https://in-n-out-3d.github.io/>

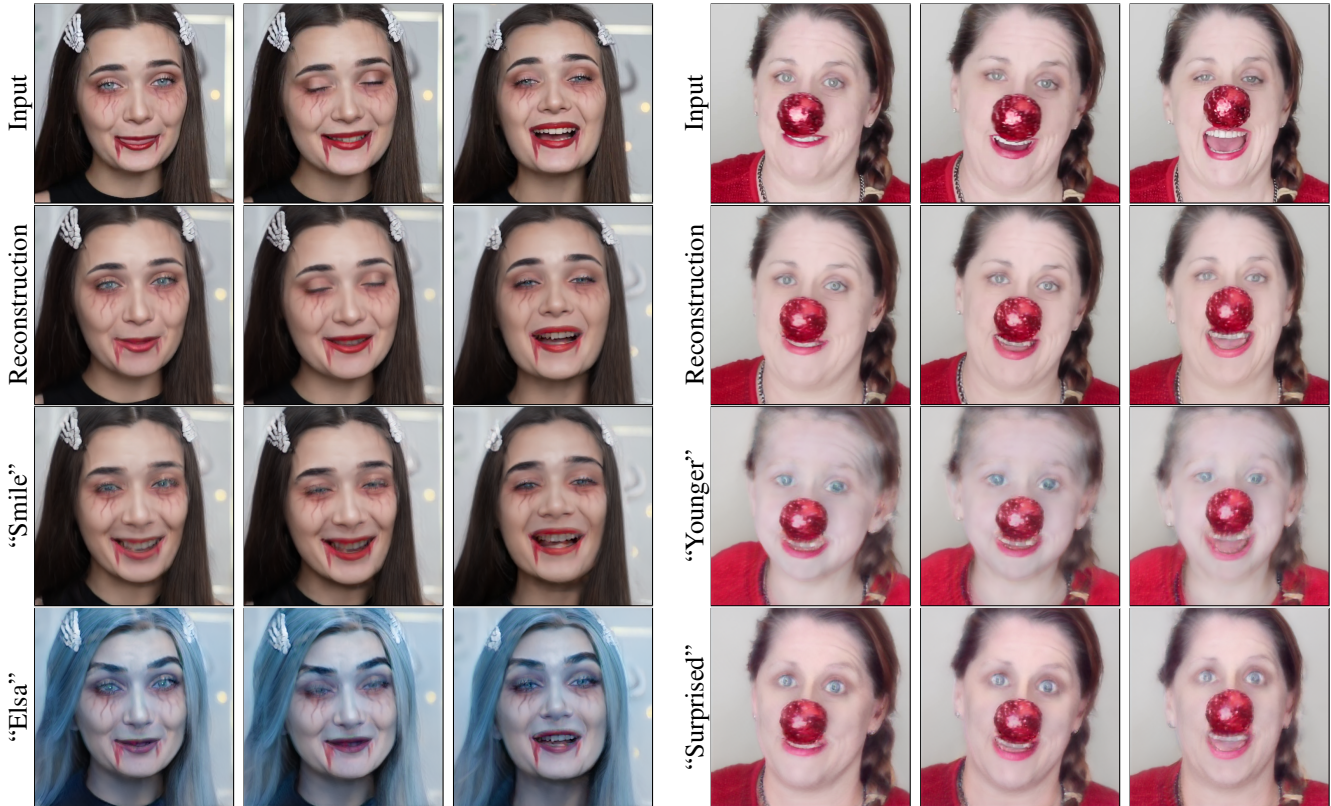


Figure 1. **Semantic editing for out-of-distribution data.** We present a method for reconstructing and editing an out-of-distribution video using a pre-trained 3D-aware generative model (EG3D [9]). Our method explicitly model and reconstruct the disoccluders in 3D, allowing faithful reconstruction of the input video while preserving the semantic editing capability. Here we showcase the reconstruction and editing results “Smile”, “Younger” [45], “Elsa”, “Surprised” [40].

## Abstract

3D-aware GANs offer new capabilities for creative content editing, such as view synthesis, while preserving the editing capability of their 2D counterparts. These methods use GAN inversion to reconstruct images or videos by optimizing a latent code, allowing for semantic editing by manipulating the code. However, a model pre-trained on a face dataset (e.g., FFHQ) often has difficulty handling faces with out-of-distribution (OOD) objects, e.g., heavy make-up or occlusions. We address this issue by explicitly modeling OOD objects in face videos. Our core idea

is to represent the face in a video using two neural radiance fields, one for the in-distribution and the other for the out-of-distribution object, and compose them together for reconstruction. Such explicit decomposition alleviates the inherent trade-off between reconstruction fidelity and editability. We evaluate our method’s reconstruction accuracy and editability on challenging real videos and showcase favorable results against other baselines.

## 1. Introduction

**GAN-based image/video editing.** *GAN inversion* [57, 64, 3, 42, 52] projects a real image onto the latent space of a pre-trained GAN to obtain a latent code (so that the input image can be reconstructed by feeding the latent code into a pre-trained GAN). By changing the latent code, one can achieve many creative semantic editing effects [45, 24, 40, 18] for images. For the video domain, recent methods also achieve faithful and temporally consistent editing [60, 53, 58]. However, these *2D methods* often lack explicit viewpoint control of the generated contents.

**3D-aware GANs.** With the rapid development of 3D reconstruction and representations [35, 6, 36, 11], high-quality 3D-aware GANs [21, 39, 9] have emerged as a powerful tool for 3D content generation. Equipped with a 3D representation (*e.g.*, neural radiance field [21, 9] or SDF [39]), these methods first render a low-resolution feature map and RGB image, followed by an upsampler to yield a high-resolution image. 3D-aware GANs offer explicit camera pose control and 3D geometry consistency while inheriting the generation capacity and editability of 2D GANs [28, 29, 26, 27]. This enables applications such as novel view synthesis and image/video editing [31, 48]. To accurately reconstruct a face’s 3D geometry and texture, using more frames or viewpoints from a face video is necessary.

**Core challenges.** We aim to develop a *3D-aware video editing* system that can be applied to in-the-wild Internet videos. Given a video, our main challenge is dealing with *out-of-distribution (OOD)* objects, *e.g.*, heavy make-ups or occlusions, because a) GAN is pre-trained only on natural faces, absent of complicated texture or large occlusion, and b) the editability performance drops significantly when we force a pre-trained GAN to model OOD objects. This is commonly known as the *reconstruction-editability trade-off* [52]. Existing GAN inversion methods assume that a *single* corresponding latent code for the input frame can be found in the latent space [47, 57], *i.e.*, they reconstruct the in-distribution natural face and the OOD objects *together*. Since an OOD object cannot be represented by a single latent code, existing methods either cannot reconstruct them faithfully [48] or can reconstruct them (through fine-tuning the generator) but sacrifice the editability [43] (Figure 2).

**Our work.** We propose a new perspective to resolve the issue by drawing inspiration from recent composite volume rendering works that compose multiple radiance fields during rendering [33, 19, 59, 55]. Our core idea is to *decompose* the 3D representation of the video with the OOD object into an *in-distribution* part and an *out-of-distribution* part, and compose them together to reconstruct the video in a composite volumetric rendering manner. We use EG3D [9] as our 3D-aware GAN backbone and leverage

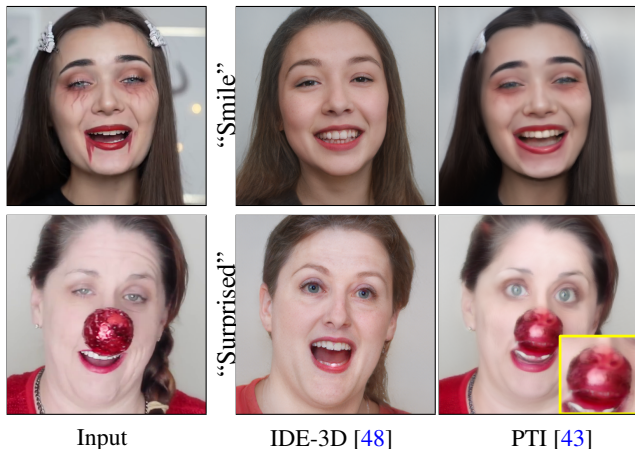


Figure 2. **Motivation.** GAN inversion techniques cannot deal with frames with OOD elements. IDE-3D [48] can produce faithful editing, but fails to preserve the identity of the input face. PTI [43] provides higher reconstruction fieldity, but the edibility suffers.

its tri-plane representation to model this composed rendering pipeline. For the in-distribution component (*i.e.* natural face), we project pixels onto EG3D’s  $\mathcal{W}^+$  space. For the out-of-distribution part, we use an additional tri-plane to represent it. Later, we combine these two radiance fields in a composite volumetric rendering to reconstruct the input frames. During the editing stage, we edit the in-distribution part, *i.e.* the latent code  $w$ , *without* touching the OOD part. Any StyleGAN-based editing approaches [40, 45] are applicable for editing the in-distribution part. The advantages of our work are three-fold: a) by composing two parts together, we achieve a higher-fidelity reconstruction, b) by editing only the in-distribution part, we maintain the editability, and c) by leveraging 3D-aware GANs, we can render the input face video from novel viewpoints.

We evaluate our proposed method on online face videos and show improved reconstruction and editing quality than the previous methods. We demonstrate interesting 3D-aware editing results, such as semantic editing, novel view synthesis, and OOD object removal.

**Our contributions.** In sum, our contributions are:

- We propose a novel 3D-aware video editing that can manipulate monocular portrait videos with the presence of out-of-distribution objects (*e.g.*, accessories and heavy make-up). See results in Figure 1.
- We incorporate composite volume rendering into 3D-aware GAN inversion.
- Our method reconstructs 3D shapes of faces with OOD objects faithfully and demonstrates novel 3D-aware video editing applications.

## 2. Related Work

**3D-aware GANs.** StyleGANs [28, 29, 26, 27] have achieved high-quality photorealistic 2D image generation

and have been successfully applied to various image editing applications [45, 40, 18, 24]. Significant progresses have also been made to lift 2D image generation to 3D space, using various 3D representations, for both higher quality generation and to enable 3D-aware applications such as view synthesis [37, 44, 10, 16, 21, 39, 9, 48, 46, 20]. These methods usually take two stage pipeline that first renders a raw image (usually also with feature maps) in low resolution and then upsamples the rendered image to high resolution. We leverage EG3D [9] as our generator architecture in this work. EG3D builds upon a StyleGAN2 [29] backbone architecture and nicely inherits the qualities of a well-behaved latent space that naturally allows effective GAN inversion and editing applications.

**GAN inversion and editing.** GAN inversion has been widely studied for 2D GANs. These techniques can largely be categorized as (a) encoder-based methods [32, 51, 38, 54, 42, 4, 52, 8, 42, 52] in which a neural network encoder is trained to project an input image to the latent space of the generator; (b) optimization-based methods [41, 1, 2, 25, 50, 22, 13, 14] where the latent code is recovered via optimizing loss functions between the generator output and a target image; and (c) hybrid methods [65, 7, 43, 5] which combine both approaches. Some recent works [31, 48, 62] have also investigated 3D-aware GAN inversion. Unlike previous methods focusing on single-image inversion, we consider multi-shot (or video) inversion. With video input, our approach can better reconstruct 3D shapes. More importantly, we propose a new mechanism to allow high-quality 3D-aware GAN inversion of *out-of-distribution faces* even with significant occlusion. As demonstrated in the experiments, previous approaches have difficulty handling these challenging cases. With our GAN inversion, we can modify the latent code to perform high-quality semantic image editing [45, 24, 40, 18] or video editing [60, 53, 58].

**GAN inversion for out-of-distribution (OOD) data.** There have been attempts to invert out-of-distribution data to the GAN’s latent space. Early work [1] proposes to project an image onto extended  $\mathcal{W}^+$  space to achieve better reconstruction. PTI [43] fine-tunes generator with regularization for lower distortion error. StyleSpace [56] proposes to invert an image using StyleGAN’s internal feature maps and tRGB blocks, which shows better reconstruction and disentanglement. Recently, ChunkyGAN [47] proposes to compose multiple generated images, from multiple latent codes, with a set of segmentation masks to reconstruct an input image. With a similar goal in mind, we propose to leverage the radiance field of EG3D [9] and decompose the volumetric representation into an in-distribution part and an out-of-distribution part. In contrast to ChunkyGAN [47] that models an image as a collection of 2D segments, we model the OOD and face directly in volumetric 3D representation and merge them with composite rendering.

**Composite Neural Radiance Fields.** Neural Radiance Fields (NeRFs) [35] have shown impressive 3D reconstruction and view synthesis results. Recently, it has been shown that 3D scenes can be decomposed into different NeRFs. When multiple radiance fields are built, one can compose them together using a composite rendering manner [33, 19, 59, 55]. Our GAN backbone EG3D [9] use the tri-plane representation to generate 3D object from the latent code. We adopt the idea of composite volume rendering to address the out-of-distribution 3D GAN inversion problem. Specifically, we split the in-distribution and out-of-distribution parts in the tri-plane 3D representation and compose them during volume rendering.

### 3. Background

#### 3.1. Neural Radiance Fields (NeRFs)

Our goal is to leverage the composability of Neural Radiance Fields [33] (NeRFs) to reconstruct the OOD object and in-distribution face, respectively. A NeRF is an implicit 3D representation with a differentiable and continuous function  $D$  (either an MLP or voxel grid features), that takes a 3D position  $\mathbf{x} \in \mathbb{R}^3$  and a view direction  $\mathbf{d} \in \mathbb{R}^3$  as the input, and outputs pointwise RGB color  $\mathbf{c} \in \mathbb{R}^3$  and density  $\sigma$ .

$$\mathbf{c}(\mathbf{x}, \mathbf{d}), \sigma(\mathbf{x}) = D(\mathbf{x}, \mathbf{d}). \quad (1)$$

To compute the color of a pixel, a ray  $\mathbf{r}(t_k) = \mathbf{o} + t_k \mathbf{d}$  is cast through the camera origin in the direction  $\mathbf{d}$ . Then, the predicted color is computed by volume rendering [34].

$$\mathbf{C}(\mathbf{r}) = \sum_{k=1}^K T(t_k) \alpha(\sigma(t_k) \delta_k) \mathbf{c}(t_k), \quad (2)$$

where  $T(t_k) = \exp(-\sum_{k'=1}^{k-1} \sigma(t_{k'}) \delta_{k'})$ ,  $\alpha = 1 - \exp(-x)$ , and  $\delta_k = t_{k+1} - t_k$  is the distance between two 3D points.

#### 3.2. 3D-aware GAN: EG3D

We choose EG3D [9], which consists of a tri-plane representation and a super-resolution (SR) module, as the 3D-aware GAN backbone.

**Neural rendering at low resolution.** Given a latent code  $z \in \mathbb{R}^{512}$  and camera parameters  $p$ , EG3D first generates a corresponding tri-plane  $\mathbf{T} \in \mathbb{R}^{256 \times 256 \times 32 \times 3}$ . For each pixel, a ray  $\mathbf{r}$  is cast, and points are sampled along the ray. Unlike the positional encoding [33, 49] for each point in NeRFs, EG3D projects each point onto  $\mathbf{T}$  and retrieves features from three planes via bilinear interpolation. These features are then aggregated by summation, and fed into the decoder  $D$  (*i.e.* an MLP) to predict the color and density. Volume rendering is then performed to compute the final color for each pixel. To this end, a raw RGB image with a

32-channel feature in a low resolution (e.g.  $128 \times 128$ ) is generated.

**Super resolution (SR).** To gain high-resolution outputs, EG3D later uses an SR module that inputs the raw image and the 32-channel feature as the input and yields a high-resolution RGB image (e.g.  $512 \times 512$ ). We build our approach upon EG3D due to its rendering efficiency compared to other alternatives [39, 21].

## 4. Method

Given an aligned, monocular face video  $\mathbf{V} = [\mathbf{I}_1, \dots, \mathbf{I}_t, \dots, \mathbf{I}_N]$  with  $N$  frames, we aim to reconstruct the video with EG3D inversion and perform face editing.

We show the high-level overview in Figure 3. Each time we sample one single frame  $\mathbf{I}_t$  from the video  $\mathbf{V}$ . Our method is unsupervised, *i.e.*, no need for segmentation masks like previous methods [19, 59]. We aim to build *two* neural radiance fields (NeRFs) [35], one for *in-distribution* face (Section 4.1), and the other one for *out-of-distribution* (OOD) object (Section 4.2), using tri-plane representations [9]. The OOD object, for example, can be a non-face object with a rigid shape or heavy makeup with a complicated texture. Next, we combine two radiance fields (Section 4.3) to reconstruct the low-resolution frame. Finally, we finetune the super-resolution module of EG3D to get the high-resolution output (Section 4.5). After training the radiance fields, we can edit the face video (Section 4.6).

### 4.1. In-distribution GAN inversion

EG3D [9]  $G$  first takes a latent code  $w \in \mathbb{R}^{14 \times 512}$  as the input to generate a tri-plane representation  $\mathbf{T}^I \in \mathbb{R}^{256 \times 256 \times 32 \times 3}$ . Then the features are sampled from  $\mathbf{T}^I$  and fed into an MLP decoder  $D^I$ . The decoder predicts the colors  $\mathbf{c}^I$  and densities  $\sigma^I$  for the 3D coordinates. Next, volume rendering [34] is used to generate a low-resolution output ( $128 \times 128$ ).

**Formulation.** The in-distribution inversion is similar to the normal 3D GAN inversion [31, 57] except we are inverting a face *video* (or multiple images of the same identity). For each frame, we optimize a latent code  $w_t$ , such that we can reconstruct the input frame  $\mathbf{I}_t$ . For camera parameters  $p_t \in \mathbb{R}^{25}$ , we obtain them by using an off-the-shelf pose detector [17], following [9, 31].

As the input video  $\mathbf{V}$  contains the face of a single identity, we use this multi-view information to recover the face details in 3D. To this end, instead of optimizing each frame’s latent code *independently*, we propose to represent each frame’s latent code using a canonical latent code  $w^{cano}$ , and a residual latent code  $w_t^{res}$ , such that

$$w_t = w^{cano} + aw_t^{res}, \quad (3)$$

where  $a$  is a factor to control the strength of the residual.

In practice, we use  $a = 0.7$ . The benefit of this is that the canonical latent code  $w^{cano}$  is shared with all the frames, containing the common representation for the same identity. The residual latent code  $w_t^{res}$  acts as a deformation upon the canonical frame. During the optimization, we back-propagate gradients to  $w_t^{cano}$  and  $w_t^{res}$ .

**Optimization.** To represent the in-distribution faces with  $\mathbf{T}^I$ , our insight is to keep  $w_t$  in distribution as much as possible. To this end, we use a regularization term to keep  $w_t$  within its pre-trained distribution through GAN training.

$$\mathcal{L}_w(w_t) = \|w_t - \bar{w}\|_2^2, \quad (4)$$

where  $\bar{w}$  is the mean latent code computed over 10,000 sampled latent codes.

We also use another regularization term adopted from [52] to constrain the variation among style vectors in  $w$ :  $\mathcal{L}_\Delta(w_t) = \sum_{i=1}^{13} \|\Delta_i\|_2^2$ , given a latent code  $w = (w_0, w_0 + \Delta_1, \dots, w_0 + \Delta_{13}) \in \mathbb{R}^{14 \times 512}$ . This regularization term preserves the editability of the optimized latent code [52].

### 4.2. Modeling out-of-distribution contents

We use an additional tri-plane  $\mathbf{T}^O$  to represent the out-of-distribution objects. However, because the object is not static across different frames, it is challenging to reconstruct it with a static radiance field. Therefore, in addition to  $\mathbf{T}^O$ , we use a time-varying latent code  $\phi_t \in \mathbb{R}^{32}$  for each frame to represent the out-of-distribution object across the temporal domain. Both  $\mathbf{T}^O$  and  $\phi_t$  are randomly initialized from a normal distribution.

**Formulation.** The out-of-distribution decoder  $D^O$  takes a tuple  $(\mathbf{T}^O(t_k), \phi_t) \in \mathbb{R}^{64}$  as the input, and outputs color  $\mathbf{c}^O \in \mathbb{R}^3$ , density  $\sigma^O \in \mathbb{R}$ , and blending weight  $b \in [0, 1]$ .

$$(\mathbf{c}^O, \sigma^O, b) = D^O(\mathbf{T}^O(t_k), \phi_t; \theta_{D^O}), \quad (5)$$

where  $\mathbf{T}^O(t_k) \in \mathbb{R}^{32}$  is the aggregated features obtained by projecting 3D coordinate  $t_k$  onto each of the three feature planes via bilinear interpolation, then aggregated via summation [9]. The decoder  $D^O$  is an MLP with weights of  $\theta_{D^O}$ . To compute the color of a pixel at time  $t$ , we use the volume rendering integral along the ray  $\mathbf{r}$ :

$$\mathbf{C}^O(\mathbf{r}) = \sum_{k=1}^K T(t_k) \alpha^O(\sigma^O(t_k) \delta_k) \mathbf{c}^O(t_k). \quad (6)$$

### 4.3. Composite volume rendering

Now with in-distribution and out-of-distribution radiance fields, we can compose them together using the blending weight  $b$  from Eqn. 5.

**Formulation.** We compose two radiance fields together by

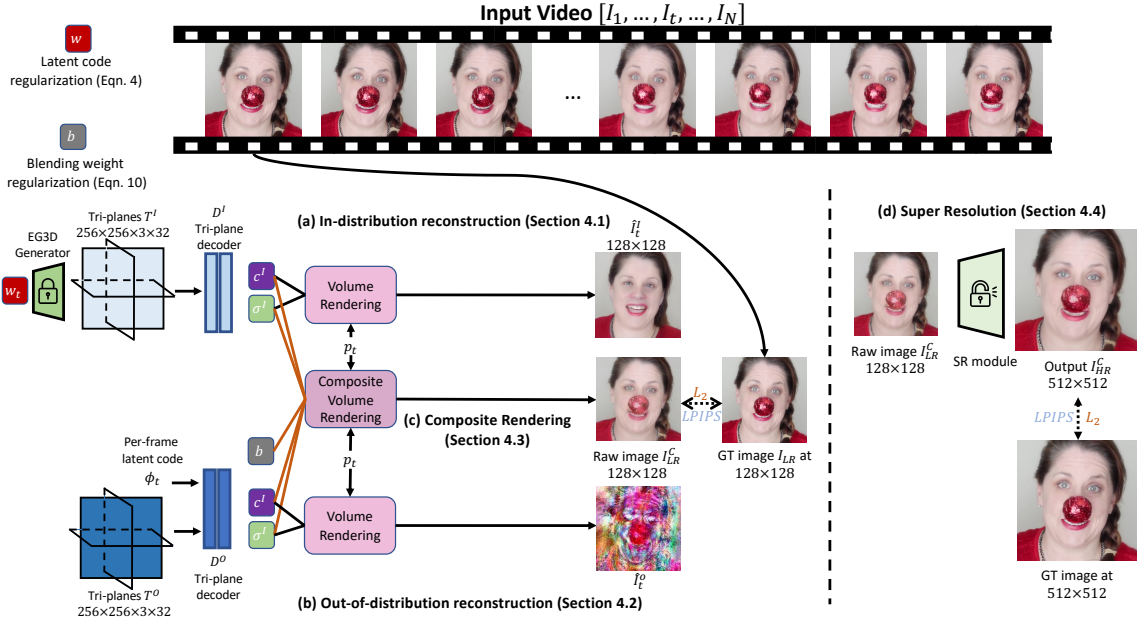


Figure 3. **Overview of our method.** Given a monocular portrait video, we use two radiance fields to represent (a) *in-distribution* face, and (b) *out-of-distribution* (OOD) item. (a) **In-distribution reconstruction** is the *GAN inversion* for the in-distribution natural face. We apply GAN inversion by using pre-trained EG3D model  $G$  to each frame, where the pre-trained tri-plane generator and tri-plane decoder  $D^I$  are kept frozen. (b) For **out-of-distribution** elements, we propose to model them with a separate radiance field represented by an additional tri-plane  $T^O$ . During the training process, we optimize the tri-plane  $T^O$ , a per-frame latent code  $\phi_t$ , and a new decoder  $D^O$ . The decoder takes as input tri-plane features  $T^O$  and  $\phi_t$  and outputs color  $c^O$ , density  $\sigma^O$ , and blending weight  $b$ . (c) **Composite Rendering** compose the *in-distribution* and *out-of-distribution* radiance fields together by using a composite rendering scheme (Section 4.3). (d) Finally, we finetune the **Super Resolution** module in  $G$  to achieve a better output in the high resolution. After training, we can perform various semantic edits and free-view rendering, while preserving the face identity and the OOD components.

$$\mathbf{C}^C(\mathbf{r}) = \sum_{k=1}^K T^C(t_k) \left( b \alpha^O(\sigma^O(t_k) \delta_k) \mathbf{c}^O(t_k) + (1-b) \alpha^I(\sigma^I(t_k) \delta_k) \mathbf{c}^I(t_k) \right), \quad (7)$$

where  $T^C(t_k) = \exp(-\sum_{k'=1}^{k-1} (\sigma^O + \sigma^I) \delta_{k'})$ .

**Optimization.** The goal is

$$\begin{aligned} \mathbf{T}^{O*}, \theta_{D^O}^*, \phi_t^* &= \underset{\mathbf{T}^O, \theta_{D^O}, \phi_t}{\operatorname{argmin}} \mathcal{L}_t^C \\ &= \underset{\mathbf{T}^O, \theta_{D^O}, \phi_t}{\operatorname{argmin}} \sum_{ij} \|\mathbf{C}^C(\mathbf{r}_{ij}) - \mathbf{C}^{GT}(\mathbf{r}_{ij})\|_2^2 \\ &\quad + \lambda_b \mathcal{L}_b(\mathbf{r}_{ij}) + \mathcal{L}_{LPIPS}(\mathbf{I}_{LR}^C, \mathbf{I}_{LR}), \end{aligned} \quad (8)$$

where  $\mathcal{L}_{LPIPS}$  is LPIPS loss [63],  $\mathbf{I}_{LR}^C$  is the composite rendered image at low resolution ( $128 \times 128$ ),  $\mathbf{I}_{LR}$  is the ground truth image also at  $128 \times 128$ . The weight regularizer  $\mathcal{L}_b$  is adopted from [55], used to penalize the blending weight  $b$  if it is not closer to 0 or 1:

$$\mathcal{L}_b(\mathbf{r}) = \sum_{k=1}^K H_b(b(t_k)), \quad (9)$$

where  $H_b(x) = -(x \log(x) + (1-x) \log(1-x))$  is binary entropy. The reason behind Eqn. 18 is that objects cannot co-occupy the same spatial location. The entropy loss facilitates a cleaner decomposition to be either an in-distribution object (*i.e.*  $b \rightarrow 0$ ) or an out-of-distribution object (*i.e.*  $b \rightarrow 1$ ).

#### 4.4. Low-resolution reconstruction

In practice, we jointly optimize for  $w_t$  (yielding  $T^I$ ),  $T^O$ ,  $\theta_{D^O}$ ,  $\phi_t$ , following Section 4.1 to Section 4.3. The total loss function is

$$\mathcal{L}^{LR} = \sum_{t=1}^N \mathcal{L}_t^C + \lambda_\Delta \mathcal{L}_\Delta + \lambda_w \mathcal{L}_w, \quad (10)$$

where  $\mathcal{L}_t^C$  is from Eqn. 7, latent variation regularizer  $\mathcal{L}_\Delta$  from [52], and  $\mathcal{L}_w$  from Eqn. 4, respectively,  $\lambda_\Delta$  is the weight for  $\mathcal{L}_\Delta$ , and  $\lambda_w$  is the weight for  $\mathcal{L}_w$ .

#### 4.5. Super resolution

After training in Section 4.1, 4.2, 4.3 and 4.4, we can get reconstruction  $\mathbf{I}_{LR}^C$  in low resolution ( $128 \times 128$ ). We ob-

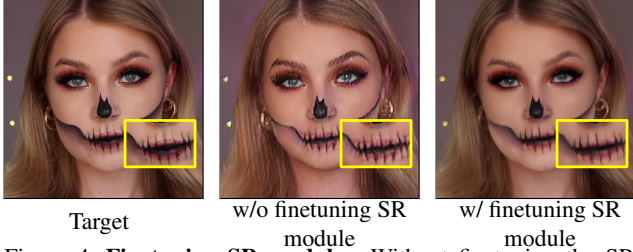


Figure 4. **Finetuning SR module.** Without finetuning the SR module, the output in high resolution ( $512 \times 512$ ) is blurry.

serve that using the pretrained super-resolution (SR) module cannot provide a good high-resolution output as shown in Figure 4. Therefore, we finetune only the SR module in  $G$  for higher resolution at  $512 \times 512$ .

**Optimization.** The loss function is that

$$\mathcal{L}^{SR}(\mathbf{x}, \hat{\mathbf{x}}) = \|\mathbf{x} - \hat{\mathbf{x}}\|_2^2 + \mathcal{L}_{LPIPS}(\mathbf{x}, \hat{\mathbf{x}}), \quad (11)$$

where  $\mathbf{x} = \mathbf{I}_t$  and  $\hat{\mathbf{x}} = SR(\mathbf{I}_{LR}^C)$ .

## 4.6. Editing

After the reconstruction, we can modify the latent code  $w_t$  to achieve semantic editing. With explicit decomposition, the out-of-distribution contents do not interfere with the semantic editing capability of in-distribution components. Here, any existing GAN-based editing approaches can be used. In our experiments, we use InterfaceGAN [45] and StyleCLIP [40].

## 5. Experimental Results

### 5.1. Experimental Setup

**Dataset.** To evaluate how our approach works on real videos with out-of-distribution objects, we collect 20 online videos as our dataset. The OOD objects contain heavy make-up, and occlusions (*e.g.* facial masks and big glasses). For the face alignment, we use 3DDFA-v2 [23] to get the 68-point landmarks and smooth them across the frames using a sliding window for stabler cropping. After that, we convert them to EG3D’s 5-point landmarks and crop the face out of the input frame.

**Hyperparameters.** We use the Adam optimizer [30] for all the experiments. For in-distribution inversion (Section 4.1), we optimize for 200 epochs with a learning rate of  $1 \times 10^{-3}$ ,  $\lambda_{\Delta} = 1 \times 10^{-3}$ . For the out-of-distribution and composite rendering (Section 4.2, 4.3), we run the optimization for 10,000 iterations with a learning rate of  $5 \times 10^{-3}$ ,  $\lambda_b = 1$ , and  $\lambda_w = 1$ . For the SR module (Section 4.5), we fine-tune the module for 100 epochs with a learning rate of  $1 \times 10^{-3}$ .

**Metrics.** We evaluate our approach from two aspects: 1) reconstruction accuracy and 2) editability to show the

reconstruction-editability trade-off. For the reconstruction accuracy, we evaluate LPIPS [63],  $\mathcal{L}_2$ , PSNR, SSIM and ID similarity [15]. For editability, we follow [43, 47] and evaluate identity preservation after applying the editing direction. After the editing, we use ArcFace [15] to compute the similarity between the inverted and edited results.

### 5.2. Quantitative results

**Reconstruction.** We compare the reconstruction accuracy of our approach with a) hybrid method: PTI [43], b) optimization-based methods:  $\mathcal{W}^+$  and  $\mathcal{W}$  optimization, and c) encoder-based method: IDE-3D [48]. For PTI, we first perform a  $\mathcal{W}^+$  inversion with a learning rate of  $1 \times 10^{-3}$  and 200 epochs. We then fine-tune the generator for 200 epochs with a learning rate of  $3 \times 10^{-5}$ . For  $\mathcal{W}^+$  and  $\mathcal{W}$  optimization, we use a learning rate of  $1 \times 10^{-3}$  and optimize for 200 epochs. For IDE-3D, we use their encoder directly for the inversion.

Table 1. Quantitative comparison for reconstruction quality.

Metrics	LPIPS↓	$\mathcal{L}_2$ ↓	SSIM↑	PSNR↑	ID similarity↑
Ours	<b>0.2237</b>	<b>0.0339</b>	<b>0.7052</b>	<b>16.0287</b>	<b>0.9758</b>
PTI [43]	0.3144	0.0504	0.6320	13.4483	0.9658
IDE-3D [48]	0.4999	0.1172	0.4512	9.5852	0.8251
$\mathcal{W}^+$	0.3380	0.0383	0.6557	14.7486	0.9154
$\mathcal{W}$	0.4030	0.0618	0.5787	12.4769	0.8652

We report the results in Table 5. Our approach outperforms other methods by a large margin on all the evaluation metrics. This indicates that our method produces a more accurate reconstruction of the OOD videos.

**Editability.** We acquire editing directions from InterfaceGAN [45] (“younger”, “smile”) and StyleCLIP mapper [40] (“eyeglasses”, “surprised”, “Elsa”). Following previous work [43, 47], we measure the ID similarity between the inverted image and the edited image, as the editing should not change a person’s identity. We report our results in Table 6. Our method outperforms other baselines in terms of identity preservation in most cases.

Table 2. Quantitative comparison for identity preservation after editing. Higher numbers indicate better identity preservation.

	“eyeglasses”	“surprised”	“younger”	“smile”	“Elsa”
Ours	<b>0.9158</b>	<b>0.9360</b>	<b>0.9347</b>	0.9094	<b>0.8927</b>
PTI	0.9049	0.9357	0.9319	<b>0.9336</b>	0.7945
IDE-3D	0.8767	0.9481	0.8551	0.8662	0.7871
$\mathcal{W}^+$	0.8971	0.9249	0.9290	0.9170	0.7968
$\mathcal{W}$	0.8793	0.9537	0.9068	0.9208	0.8113

### 5.3. Qualitative results

**Inversion.** We show a visual comparison regarding the reconstruction with PTI [43], IDE-3D [48],  $\mathcal{W}^+$  and  $\mathcal{W}$  in Figure 5. Our method provides higher-fidelity reconstruction results than other baselines, particularly for

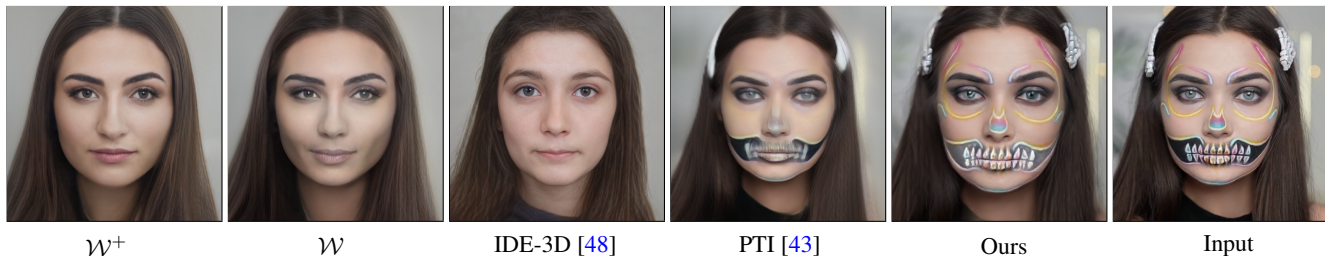


Figure 5. **Qualitative comparison of the reconstruction.** We compare our approach with  $\mathcal{W}^+$  and  $\mathcal{W}$  optimization, IDE-3D [48], and PTI [43]. Our method shows a better reconstruction accuracy on the OOD videos.

OOD regions (e.g., heavy make-up or earrings). Compared to encoder-based method IDE-3D, our method shows more consistent results with less flickering. Compared to optimization-based methods,  $\mathcal{W}$ ,  $\mathcal{W}^+$ , and the hybrid method, PTI, our method shows higher-fidelity reconstruction for OOD objects (Refer to our supplementary material for video comparison).

**Editing.** We show a qualitative comparison regarding the editing in Figure 6. Our method shows faithful editing results and less temporal flickering than other baselines. For more qualitative results, please refer to our supplementary material.

#### 5.4. Other Applications

**View synthesis.** The use of 3D GANs supports rendering novel views after inversion. We show novel view synthesis results in Figure 7. Our method can generate 3D consistent novel views *both* for the face and OOD object.

**Object removal.** By setting the blending weights of the OOD objects to 0, we can remove OOD objects. We show results in Figure 8.

#### 5.5. Ablation Study

We introduce two loss functions, Eqn. 4 and Eqn. 18, to preserve the editability from the impact of the OOD radiance field in Section 4.3. To validate the loss functions' effects, we conduct an ablation study in Table 3. Without the weight regularization,  $\mathcal{L}_b$  and latent code regularizer  $\mathcal{L}_w$ , the reconstruction accuracy is improved while the editability is reduced. One of the reasons is that GAN-based editing usually also brings unwanted changes to other attributes [45]. In Figure 9, the editing direction "eyeglasses" also moves the position of the eyes. At this time, if the blending weight  $b$  is closer to 1 for pixels outside the OOD object, *i.e.* the OOD part has more contributions, the editing tends to keep the pixel values in the reconstruction stage. While the eyes will be moved due to the editing direction, it results in the duplicate eyes in Figure 9. In contrast, with regularization (Eqn. 4 and Eqn. 18) on the blending weights, pixels in the in-distribution part contribute more to the output, which better supports the editing since we can only edit the in-distribution part.

Table 3. Ablation study.

	Inversion		Editing
	$\mathcal{L}_2 \downarrow$	LPIPS $\downarrow$	ID similarity $\uparrow$
w/o $\mathcal{L}_b$ and $\mathcal{L}_w$	0.0362	0.2339	0.8826
w/o $\mathcal{L}_b$	<b>0.0322</b>	<b>0.2191</b>	0.9070
w/o $\mathcal{L}_w$	0.0336	0.2238	0.9024
Full method	0.0339	0.2237	<b>0.9177</b>

#### 5.6. Speed

We include a comparison of different baselines in Table 7. We compare the speed on 200 frames using a single NVIDIA RTX A4000 GPU. Our method takes more time for optimization but gains a significant improvement over the reconstruction-editability trade-off.

Table 4. Speed for different baselines on 200 frames.

PTI [43]	IDE-3D [48]	Ours
2.18h	95s	3.17h

#### 5.7. Number of frames

The number of frames needed for reconstructing OOD objects depends on the number of viewpoints of the OOD object shown in a video. Our method usually takes 30-100 frames for a natural talking video. Compared to encoder-based method IDE-3D [48], our method needs more frames, but we show a higher-fidelity reconstruction and editing performance. Compared to optimization-based methods  $\mathcal{W}$ ,  $\mathcal{W}^+$ , and hybrid method PTI [43], we use the same frames as they do, but we show more accurate reconstruction and better editability in Figure 5 and Figure 6.

#### 5.8. Comparison with the supervised approach

Our framework can also work if the segmentation masks of OOD objects are given, like previous work [19]. We compare our *unsupervised* framework (Section 4) and a *semi-supervised* approach, built upon our framework, with *one* manually labeled mask of the OOD object. Please refer to our supplementary material for implementation details. We showcase a qualitative comparison in Figure 10. Compared to the semi-supervised method, the performance of our method is slightly worse, but our unsupervised approach works without segmentation masks or humans in the loop.

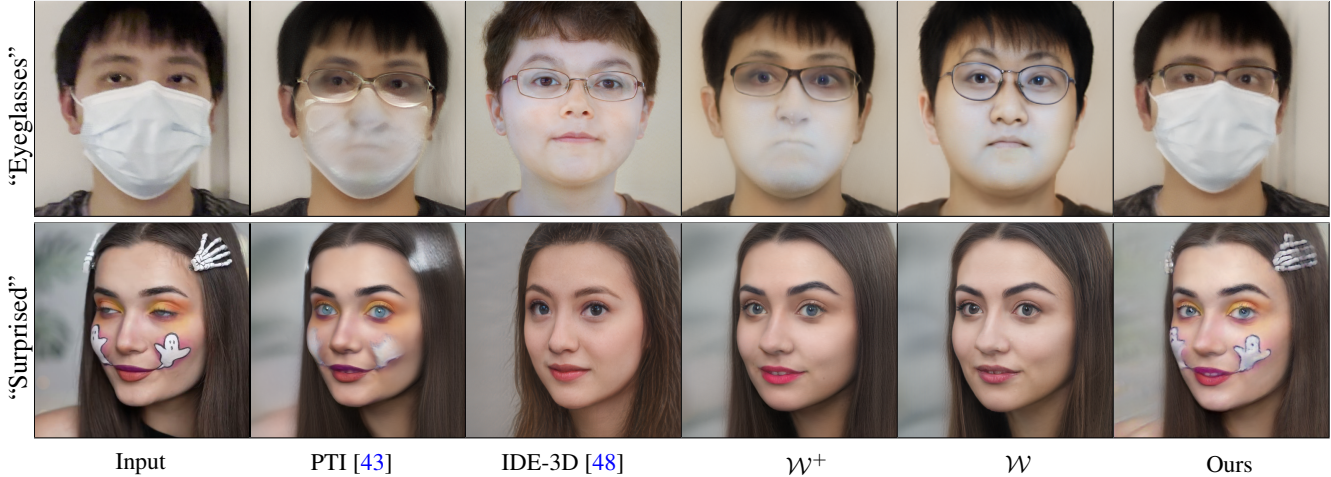


Figure 6. **Qualitative comparison of the editing.** We compare our editing results with other baselines, with different editing latent directions “Eyeglasses”, and “Surprised”. Our approach can preserve the original appearance details better, and shows improved editability over other baselines.



Figure 7. **Novel view synthesis.** We can synthesize novel views for a fixed frame in a video, which is challenging for 2D GANs. Each column shows different view for the same frame.



Figure 8. **OOD object removal.** By setting the blending weights inside the mask to 0, we can remove the OOD object.

## 6. Limitations

Our method still consists of several limitations. We visualize (a)-(c) in Figure 11.

**(a) Editing on OOD part.** When editing on the OOD region, *e.g.* adding eyeglasses to the heavy makeup region, because the blending weights are closer to 1, the eyeglasses in the in-distribution radiance field are hard to be added.

**(b) Duplicate objects.** Since our OOD radiance field has no knowledge about the GAN and faces prior, when the OOD object itself is glasses, adding eyeglasses introduces duplicate objects.

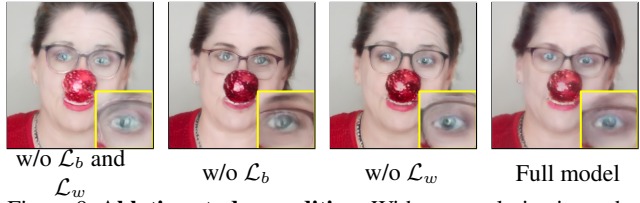


Figure 9. **Ablation study on editing.** Without regularizations, the out-of-distribution component dominates ( $b \rightarrow 1$ ) and weakens the editing. Here we show that the other results have “duplicate eyes” artifact because the editing direction “eyeglasses” is not disentangled well with other attributes, and changes the positions of the eyes, while the blending weights are the same as the reconstruction, it results in duplicated eyes. Also, with a large learning rate changes the color of the eyes.

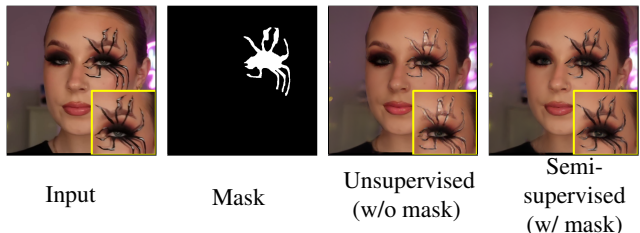


Figure 10. **Comparison between our unsupervised method and semi-supervised one.** Our unsupervised method performs slightly worse than the semi-supervised method for detailed texture.

**(c) Extreme poses.** Our method fails at editing.

**(d) Objects with limited movement.** The radiance field reconstruction suffers when the OOD object has slight movement. This may introduce unwanted artifacts like “floater” in the novel views.



(a) OOD dominates (b) Double glasses (c) Extreme pose  
 Figure 11. **Limitations.** Our approach has some limitations. (a) Editing on where OOD blending weights dominate is challenging, (b) Adding another eyeglasses to OOD eyeglasses will result in duplicated objects, and (c) extreme poses.

## 7. Conclusions

We have presented a novel method for face video inversion and editing. Our method handles out-of-distribution objects by isolating them from the in-distribution part. Our method achieves accurate reconstruction by building two radiance fields and then composing them together during the rendering. Then by modifying the latent code in the in-distribution part, we can obtain plausible editing results. We show that our method achieves a better balance in the reconstruction-editability trade-off than other baselines.

**Social impacts.** Malicious use of our technique may lead to misinformation.

## References

- [1] Rameen Abdal, Yipeng Qin, and Peter Wonka. Image2stylegan: How to embed images into the stylegan latent space? In *ICCV*, 2019. 3
- [2] Rameen Abdal, Yipeng Qin, and Peter Wonka. Image2stylegan++: How to edit the embedded images? In *CVPR*, 2020. 3
- [3] Rameen Abdal, Peihao Zhu, Niloy J Mitra, and Peter Wonka. Styleflow: Attribute-conditioned exploration of stylegan-generated images using conditional continuous normalizing flows. *ACM Transactions on Graphics (ToG)*, 40(3):1–21, 2021. 2
- [4] Yuval Alaluf, Or Patashnik, and Daniel Cohen-Or. Restyle: A residual-based stylegan encoder via iterative refinement. In *ICCV*, 2021. 3
- [5] Yuval Alaluf, Omer Tov, Ron Mokady, Rinon Gal, and Amit Bermano. Hyperstyle: Stylegan inversion with hypernetworks for real image editing. In *CVPR*, 2022. 3
- [6] Jonathan T Barron, Ben Mildenhall, Matthew Tancik, Peter Hedman, Ricardo Martin-Brualla, and Pratul P Srinivasan. Mip-nerf: A multiscale representation for anti-aliasing neural radiance fields. In *ICCV*, 2021. 2
- [7] David Bau, Hendrik Strobelt, William Peebles, Bolei Zhou, Jun-Yan Zhu, Antonio Torralba, et al. Semantic photo manipulation with a generative image prior. *ACM Transactions on Graphics (ToG)*, 38(4):1–11, 2020. 3
- [8] Lucy Chai, Jonas Wulff, and Phillip Isola. Using latent space regression to analyze and leverage compositionality in gans. In *ICLR*, 2021. 3
- [9] Eric R Chan, Connor Z Lin, Matthew A Chan, Koki Nagano, Boxiao Pan, Shalini De Mello, Orazio Gallo, Leonidas J Guibas, Jonathan Tremblay, Sameh Khamis, et al. Efficient geometry-aware 3d generative adversarial networks. In *CVPR*, 2022. 1, 2, 3, 4, 12, 13
- [10] Eric R Chan, Marco Monteiro, Petr Kellnhofer, Jiajun Wu, and Gordon Wetzstein. pi-gan: Periodic implicit generative adversarial networks for 3d-aware image synthesis. In *CVPR*, 2021. 3
- [11] Anpei Chen, Zexiang Xu, Andreas Geiger, Jingyi Yu, and Hao Su. Tensorf: Tensorial radiance fields. In *ECCV*, 2022. 2
- [12] Ho Kei Cheng and Alexander G Schwing. Xmem: Long-term video object segmentation with an atkinson-shiffrin memory model. In *ECCV*, 2022. 12
- [13] Edo Collins, Raja Bala, Bob Price, and Sabine Susstrunk. Editing in style: Uncovering the local semantics of gans. In *CVPR*, 2020. 3
- [14] Giannis Daras, Augustus Odena, Han Zhang, and Alexandros G Dimakis. Your local gan: Designing two dimensional local attention mechanisms for generative models. In *CVPR*, 2020. 3
- [15] Jiankang Deng, Jia Guo, Niannan Xue, and Stefanos Zafeiriou. Arcface: Additive angular margin loss for deep face recognition. In *CVPR*, 2019. 6
- [16] Yu Deng, Jiaolong Yang, Jianfeng Xiang, and Xin Tong. Gram: Generative radiance manifolds for 3d-aware image generation. In *CVPR*, 2022. 3
- [17] Yu Deng, Jiaolong Yang, Sicheng Xu, Dong Chen, Yunde Jia, and Xin Tong. Accurate 3d face reconstruction with weakly-supervised learning: From single image to image set. In *CVPR Workshops*, 2019. 4, 13
- [18] Rinon Gal, Or Patashnik, Haggai Maron, Amit H Bermano, Gal Chechik, and Daniel Cohen-Or. Stylegan-nada: Clip-guided domain adaptation of image generators. *ACM Transactions on Graphics (TOG)*, 41(4):1–13, 2022. 2, 3
- [19] Chen Gao, Ayush Saraf, Johannes Kopf, and Jia-Bin Huang. Dynamic view synthesis from dynamic monocular video. In *ICCV*, 2021. 2, 3, 4, 7, 12
- [20] Jun Gao, Tianchang Shen, Zian Wang, Wenzheng Chen, Kangxue Yin, Daiqing Li, Or Litany, Zan Gojcic, and Sanja Fidler. Get3d: A generative model of high quality 3d textured shapes learned from images. *arXiv preprint arXiv:2209.11163*, 2022. 3
- [21] Jiatao Gu, Lingjie Liu, Peng Wang, and Christian Theobalt. StyleRF: A style-based 3d aware generator for high-resolution image synthesis. In *ICLR*, 2022. 2, 3, 4
- [22] Jinjin Gu, Yujun Shen, and Bolei Zhou. Image processing using multi-code gan prior. In *CVPR*, 2020. 3
- [23] Jianzhu Guo, Xiangyu Zhu, Yang Yang, Fan Yang, Zhen Lei, and Stan Z Li. Towards fast, accurate and stable 3d dense face alignment. In *ECCV*, 2020. 6
- [24] Erik Härkönen, Aaron Hertzmann, Jaakko Lehtinen, and Sylvain Paris. Ganspace: Discovering interpretable gan controls. *Advances in Neural Information Processing Systems*, 33:9841–9850, 2020. 2, 3

- [25] Minyoung Huh, Richard Zhang, Jun-Yan Zhu, Sylvain Paris, and Aaron Hertzmann. Transforming and projecting images to class-conditional generative networks. In *ECCV*, 2020. 3
- [26] Tero Karras, Miika Aittala, Janne Hellsten, Samuli Laine, Jaakko Lehtinen, and Timo Aila. Training generative adversarial networks with limited data. *Advances in Neural Information Processing Systems*, 33:12104–12114, 2020. 2
- [27] Tero Karras, Miika Aittala, Samuli Laine, Erik Härkönen, Janne Hellsten, Jaakko Lehtinen, and Timo Aila. Alias-free generative adversarial networks. *Advances in Neural Information Processing Systems*, 34:852–863, 2021. 2
- [28] Tero Karras, Samuli Laine, and Timo Aila. A style-based generator architecture for generative adversarial networks. In *CVPR*, 2019. 2
- [29] Tero Karras, Samuli Laine, Miika Aittala, Janne Hellsten, Jaakko Lehtinen, and Timo Aila. Analyzing and improving the image quality of stylegan. In *CVPR*, 2020. 2, 3
- [30] Diederik P Kingma and Jimmy Ba. Adam: A method for stochastic optimization. *arXiv preprint arXiv:1412.6980*, 2014. 6, 12, 13, 14
- [31] Connor Z Lin, David B Lindell, Eric R Chan, and Gordon Wetzstein. 3d gan inversion for controllable portrait image animation. *arXiv preprint arXiv:2203.13441*, 2022. 2, 3, 4
- [32] Junyu Luo, Yong Xu, Chenwei Tang, and Jiancheng Lv. Learning inverse mapping by autoencoder based generative adversarial nets. In *Advances in Neural Information Processing Systems*, pages 207–216, 2017. 3
- [33] Ricardo Martin-Brualla, Noha Radwan, Mehdi SM Sajjadi, Jonathan T Barron, Alexey Dosovitskiy, and Daniel Duckworth. Nerf in the wild: Neural radiance fields for unconstrained photo collections. In *CVPR*, 2021. 2, 3
- [34] Nelson Max. Optical models for direct volume rendering. *IEEE Transactions on Visualization and Computer Graphics*, 1(2):99–108, 1995. 3, 4
- [35] Ben Mildenhall, Pratul P. Srinivasan, Matthew Tancik, Jonathan T. Barron, Ravi Ramamoorthi, and Ren Ng. Nerf: Representing scenes as neural radiance fields for view synthesis. In *ECCV*, 2020. 2, 3, 4
- [36] Thomas Müller, Alex Evans, Christoph Schied, and Alexander Keller. Instant neural graphics primitives with a multiresolution hash encoding. *ACM Trans. Graph.*, 41(4):102:1–102:15, July 2022. 2
- [37] Thu Nguyen-Phuoc, Chuan Li, Lucas Theis, Christian Richardt, and Yong-Liang Yang. Hologan: Unsupervised learning of 3d representations from natural images. In *ICCV*, 2019. 3
- [38] Yotam Nitzan, A. Bermano, Yangyan Li, and D. Cohen-Or. Face identity disentanglement via latent space mapping. *ACM Transactions on Graphics (TOG)*, 39:1–14, 2020. 3
- [39] Roy Or-El, Xuan Luo, Mengyi Shan, Eli Shechtman, Jeong Joon Park, and Ira Kemelmacher-Shlizerman. StyleSDF: High-Resolution 3D-Consistent Image and Geometry Generation. In *CVPR*, 2022. 2, 3, 4
- [40] Or Patashnik, Zongze Wu, Eli Shechtman, Daniel Cohen-Or, and Dani Lischinski. Styleclip: Text-driven manipulation of stylegan imagery. In *ICCV*, 2021. 1, 2, 3, 6
- [41] Ankit Raj, Yuqi Li, and Yoram Bresler. Gan-based projector for faster recovery with convergence guarantees in linear inverse problems. In *ICCV*, 2019. 3
- [42] Elad Richardson, Yuval Alaluf, Or Patashnik, Yotam Nitzan, Yaniv Azar, Stav Shapiro, and Daniel Cohen-Or. Encoding in style: a stylegan encoder for image-to-image translation. In *CVPR*, 2021. 2, 3
- [43] Daniel Roich, Ron Mokady, Amit H Bermano, and Daniel Cohen-Or. Pivotal tuning for latent-based editing of real images. *ACM Transactions on Graphics (TOG)*, 42(1):1–13, 2022. 2, 3, 6, 7, 8, 14
- [44] Katja Schwarz, Yiyi Liao, Michael Niemeyer, and Andreas Geiger. Graf: Generative radiance fields for 3d-aware image synthesis. *Advances in Neural Information Processing Systems*, 33:20154–20166, 2020. 3
- [45] Yujun Shen, Jinjin Gu, Xiaoou Tang, and Bolei Zhou. Interpreting the latent space of gans for semantic face editing. In *CVPR*, 2020. 1, 2, 3, 6, 7
- [46] Ivan Skorokhodov, Sergey Tulyakov, Yiqun Wang, and Peter Wonka. Epigraf: Rethinking training of 3d gans. *arXiv preprint arXiv:2206.10535*, 2022. 3
- [47] Adéla Šubrťová, David Futschik, Jan Čech, Michal Lukáč, Eli Shechtman, and Daniel Šykora. Chunkygan: Real image inversion via segments. In *European Conference on Computer Vision*, pages 189–204. Springer, 2022. 2, 3, 6
- [48] Jingxiang Sun, Xuan Wang, Yichun Shi, Lizhen Wang, Jue Wang, and Yebin Liu. Ide-3d: Interactive disentangled editing for high-resolution 3d-aware portrait synthesis. *ACM Transactions on Graphics (ToG)*, 41(6):1–10, 2022. 2, 3, 6, 7, 8, 14
- [49] Matthew Tancik, Pratul Srinivasan, Ben Mildenhall, Sara Fridovich-Keil, Nithin Raghavan, Utkarsh Singhal, Ravi Ramamoorthi, Jonathan Barron, and Ren Ng. Fourier features let networks learn high frequency functions in low dimensional domains. *Advances in Neural Information Processing Systems*, 33:7537–7547, 2020. 3
- [50] Ayush Tewari, Mohamed Elgharib, Florian Bernard, Hans-Peter Seidel, Patrick Pérez, Michael Zollhöfer, Christian Theobalt, et al. Pie: Portrait image embedding for semantic control. *arXiv preprint arXiv:2009.09485*, 2020. 3
- [51] Ayush Tewari, Mohamed Elgharib, Gaurav Bharaj, Florian Bernard, Hans-Peter Seidel, Patrick Pérez, Michael Zollhöfer, and Christian Theobalt. Stylerig: Rigging stylegan for 3d control over portrait images. In *CVPR*, 2020. 3
- [52] Omer Tov, Yuval Alaluf, Yotam Nitzan, Or Patashnik, and Daniel Cohen-Or. Designing an encoder for stylegan image manipulation. *ACM Transactions on Graphics (TOG)*, 40(4):1–14, 2021. 2, 3, 4, 5, 13
- [53] Rotem Tzaban, Ron Mokady, Rinon Gal, Amit H Bermano, and Daniel Cohen-Or. Stitch it in time: Gan-based facial editing of real videos. *SIGGRAPH Asia 2022 Conference Papers*, 2022. 2, 3
- [54] Yuri Viazovetskiy, Vladimir Ivashkin, and Evgeny Kashin. Stylegan2 distillation for feed-forward image manipulation. In *ECCV*, pages 170–186. Springer, 2020. 3
- [55] Tianhao Wu, Fangcheng Zhong, Andrea Tagliasacchi, Forrester Cole, and Cengiz Oztireli. D<sup>2</sup>nerf: Self-supervised

- decoupling of dynamic and static objects from a monocular video. *arXiv preprint arXiv:2205.15838*, 2022. [2](#), [3](#), [5](#), [14](#)
- [56] Zongze Wu, Dani Lischinski, and Eli Shechtman. Stylespace analysis: Disentangled controls for stylegan image generation. In *CVPR*, 2021. [3](#)
- [57] Weihao Xia, Yulun Zhang, Yujiu Yang, Jing-Hao Xue, Bolei Zhou, and Ming-Hsuan Yang. Gan inversion: A survey. *IEEE Transactions on Pattern Analysis and Machine Intelligence*, 2022. [2](#), [4](#)
- [58] Yiran Xu, Badour AlBahar, and Jia-Bin Huang. Temporally consistent semantic video editing. In *ECCV*, pages 357–374. Springer, 2022. [2](#), [3](#)
- [59] Bangbang Yang, Yinda Zhang, Yinghao Xu, Yijin Li, Han Zhou, Hujun Bao, Guofeng Zhang, and Zhaopeng Cui. Learning object-compositional neural radiance field for editable scene rendering. In *ICCV*, 2021. [2](#), [3](#), [4](#), [12](#)
- [60] Xu Yao, Alasdair Newson, Yann Gousseau, and Pierre Hellier. A latent transformer for disentangled face editing in images and videos. In *ICCV*, 2021. [2](#), [3](#)
- [61] Changqian Yu, Changxin Gao, Jingbo Wang, Gang Yu, Chunhua Shen, and Nong Sang. Bisenet v2: Bilateral network with guided aggregation for real-time semantic segmentation. *International Journal of Computer Vision*, 129(11):3051–3068, 2021. [12](#)
- [62] Jichao Zhang, Aliaksandr Siarohin, Yahui Liu, Hao Tang, Nicu Sebe, and Wei Wang. Training and tuning generative neural radiance fields for attribute-conditional 3d-aware face generation. *arXiv preprint arXiv:2208.12550*, 2022. [3](#)
- [63] Richard Zhang, Phillip Isola, Alexei A Efros, Eli Shechtman, and Oliver Wang. The unreasonable effectiveness of deep features as a perceptual metric. In *CVPR*, 2018. [5](#), [6](#), [13](#), [14](#)
- [64] Jiapeng Zhu, Yujun Shen, Deli Zhao, and Bolei Zhou. In-domain gan inversion for real image editing. In *European conference on computer vision*, pages 592–608. Springer, 2020. [2](#)
- [65] Jiapeng Zhu, Yujun Shen, Deli Zhao, and Bolei Zhou. In-domain gan inversion for real image editing. In *ECCV*, 2020. [3](#)

## A. Implementation details

This section discusses further details not included in the main paper due to the page limit.

### A.1. In-distribution inversion

We further present the details in Section 4.1 in the main paper.

**Latent code initialization.** Instead of initializing the latent codes  $[w_1, \dots, w_N]$ ,  $w_t \in \mathbb{R}^{14 \times 512}$  using an average latent code, we propose to use the nearest neighbor (NN) approach for the initialization. We show our approach in Algorithm 1.

---

**Algorithm 1:** NN\_init(): Nearest Neighbor (NN) Initialization for latent codes

---

**Input :** Video  $\mathbf{V} = [\mathbf{I}_1, \dots, \mathbf{I}_N]$ , pre-trained generator  $G$ , camera parameters  $[p_1, \dots, p_N]$ , perceptual loss  $LPIPS()$ , the number of samples  $n$ .

**Output:** Initialized latent codes  $[w_1, \dots, w_t]$ .

```
1 for  $t \leftarrow 1$  to  $N$  do
2    $w_{samples} = []$ 
3   Distances  $dist_s = []$ 
4   for  $i \leftarrow 1$  to  $n$  do
5     Draw  $z_i \in \mathbb{R}^{512} \sim \mathcal{N}(\mathbf{0}, \mathbf{I})$ .
6     Compute  $w_i \leftarrow G.mapping(z_i, p_t)$ 
7      $w_{samples}.insert(w_i)$ 
8      $dist_s.insert(LPIPS(G(w_i, p_t), \mathbf{I}_t))$ 
9   end
10   $w_t \leftarrow NearestNeighbor(w_{samples}, dist_s)$ 
11 end
12 Return mean( $[w_1, \dots, w_N]$ ).
```

---

**Optimization.** As mentioned in Section 4.1 in our main paper, we use a residual form to represent the latent code of each frame.

$$w_t = w^{cano} + aw_t^{res}, \quad (12)$$

where  $w^{cano}$  is the canonical latent code, and  $w_t^{res}$  is the residual. In practice, we use  $a = 0.7$ .

During the optimization, we first sample  $K = 16$  frames from the entire video. For the subset optimization, we use  $M_1 = 200$ ; to upscale the result to the whole video, we use  $M_2 = 20$ . The optimizer is Adam [30]. The learning rate is  $5 \times 10^{-3}$ . To initialize the latent codes, we randomly sample  $n = 500$  latent codes.

### A.2. Out-of-domain inversion

We further explain the details in Section 4.2 in the main paper.

**Tri-plane.** We use the Tri-plane representation from EG3D [9]. For the out-of-distribution (OOD) object, we

use tri-plane  $\mathbf{T}^O \in \mathbb{R}^{256 \times 256 \times 32 \times 3}$  as its 3D representation.  $\mathbf{T}^O$  is initialized from a standard normal distribution. Given a 3D position  $\mathbf{x} \in \mathbb{R}^3$ , we project it onto each of the plane and retrieve the corresponding feature vectors  $F_{xy}, F_{yz}, F_{xz}$  through a bilinear interpolation. Then three feature vectors are aggregated via summation.

**Per-frame latent code  $\phi_t$ .** To encode the OOD object across different frames, we use a time-varying latent code  $\phi_t \in \mathbb{R}^{32}$  for each frame. We draw  $\phi_t \sim \mathcal{N}(\mathbf{0}, \mathbf{I})$ .  $\phi_t$  is optimized together with other variables in Section 4.2.

**Decoder.** For the out-of-distribution inversion, we use a two-layer Multi-Layer Perceptron (MLP) as the decoder to predict the pointwise color  $\mathbf{c} \in \mathbb{R}^3$ , density  $\sigma \in \mathbb{R}$ , and blending weight  $b \in \mathbb{R}$  for the later composite rendering.

$$(\mathbf{c}^O, \sigma^O, b) = D^O(\mathbf{T}^O(t_k), \phi_t; \theta_{D^O}). \quad (13)$$

**Optimization.** During the optimization, we use the loss function Eqn. 7 in the main paper.

### A.3. Post-processing

We can put the aligned frames back into the original input video as an optional step. We use a face parsing algorithm [61] to get the face segmentation and paste the face back to the input frame with a Gaussian Blur to smooth the boundary. Finally, we paste the cropped, aligned frame into the full-resolution input video.

### A.4. Semi-supervised framework

Our framework can be modified to work with user-given segmentation masks like previous works on NeRFs [19, 59]. Given an aligned, monocular face video  $\mathbf{V} = [\mathbf{I}_1, \dots, \mathbf{I}_t, \dots, \mathbf{I}_N]$  with  $N$  frames, and binary masks  $[\mathbf{M}_1, \dots, \mathbf{M}_t, \dots, \mathbf{M}_N]$  of the out-of-distribution (OOD) content for each frame, we aim to reconstruct the video with EG3D inversion and perform face editing. For each video, we label the *first frame* for  $\mathbf{M}_1$ , and use an off-the-shelf tracking algorithm [12] to propagate it to obtain other masks  $\mathbf{M}$ 's. We show the overview of our semi-supervised framework in Figure 12.

**Diffrence.** The main difference between our unsupervised framework (shown in our main paper) and semi-supervised framework is that we introduce two additional reconstruction loss functions for the in-distribution radiance field and the out-of-distribution radiance field, respectively. This is because we can use 2D masks to segment the in-distribution and out-of-distribution parts.

**In-distribution radiance field.** The optimization goal for

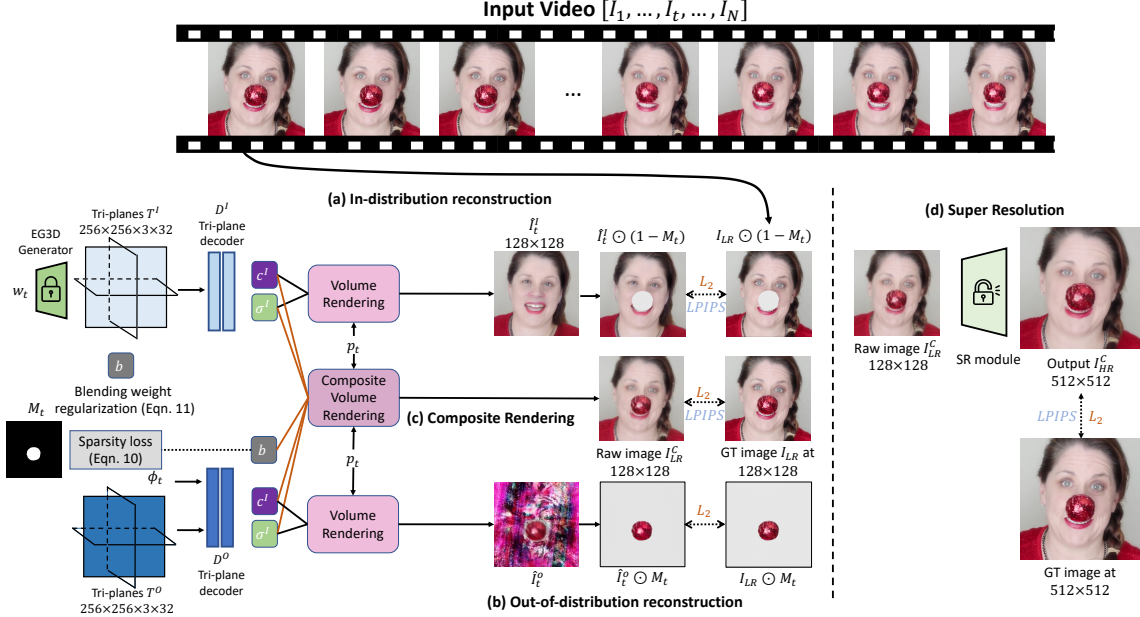


Figure 12. **Overview of our semi-supervised method.** Given a monocular portrait video, we use two radiance fields to represent (a) *in-distribution* face, and (b) *out-of-distribution (OOD)* item. (a) **In-distribution reconstruction** is the *GAN inversion* for the in-distribution face. We apply GAN inversion to each frame, but exclude the pixels within the OOD mask  $M_t$ . We perform GAN inversion by using pre-trained EG3D model  $G$ , where the pre-trained tri-plane generator and tri-plane decoder  $D^I$  are kept frozen. (b) For **out-of-distribution** elements, we propose to model them with a separate radiance field described by an additional tri-plane  $T^O$ . During the training process, we optimize the tri-plane  $T^O$ , a per-frame latent code  $\phi_t$ , and a new decoder  $D^O$  with a masked reconstruction loss. The decoder takes as input tri-plane features  $T^O$  and  $\phi_t$  and outputs color  $c^O$ , density  $\sigma^O$ , and blending weight  $b$ . (c) **Composite Rendering** compose the *in-distribution* and *out-of-distribution* radiance fields together by using a composite rendering scheme. (d) Finally, we finetune the **Super Resolution** module in  $G$  to achieve a better output in the high resolution. After training, we can perform various semantic edits and free-view rendering, while preserving the face identity and the OOD components.

the in-distribution radiance field is

$$w_t^* = \underset{w_t}{\operatorname{argmin}} \mathcal{L}_t^I = \underset{w_t}{\operatorname{argmin}} \frac{1}{\|\mathbf{m}_t\|_1} \|\mathbf{m}_t \odot (\mathbf{x} - \hat{\mathbf{x}})\|_2^2 + \mathcal{L}_{\text{mLPIPS}}(\mathbf{x}, \hat{\mathbf{x}}, \mathbf{m}_t) + \lambda_{\Delta} \mathcal{L}_{\Delta}(w_t), \quad (14)$$

where  $w_t$  is the latent code at time  $t$ ,  $\mathbf{x}$  is the input frame  $\mathbf{I}_t$ ,  $\hat{\mathbf{x}}$  is generation output  $G(w_t, p_t)$ ,  $\mathbf{m}_t = 1 - M_t$ , and  $\mathcal{L}_{\text{mLPIPS}}(x, \hat{x}, \mathbf{m})$  is the masked version of LPIPS loss [63]. Here,  $p_t$  is the camera parameters estimated by [17]. The masked LPIPS only considers features inside the mask  $\mathbf{m}$ .  $\mathcal{L}_{\Delta}(w) = \sum_{i=1}^{13} \|\Delta_i\|_2^2$  is a regularization loss adopted from [52], used to constrain the variation among style vectors in  $w$  given a latent code  $w = (w_0, w_0 + \Delta_1, \dots, w_0 + \Delta_{13}) \in \mathbb{R}^{14 \times 512}$ . By minimizing the variation, we push  $w \in \mathcal{W}^+$  to be closer to  $\mathcal{W}$  space, which has better editability.

We do not directly optimize for all the latent codes at once to speed up the optimization. Instead, we first sample a subset of frames with corresponding initial latent codes from the video. We optimize for these sampled latent codes, get the canonical latent code, and then upscale it to all the

frames for a few epochs. We find this can speed up the optimization and keep good reconstruction quality for the whole video.

We first sample  $K = 16$  frames from the whole video during our optimization. For the subset optimization, we use  $M_1 = 200$ ; to upscale the result to the whole video, we use  $M_2 = 20$ . The optimizer is Adam [30]. The learning rate is  $5 \times 10^{-3}$ . To initialize the latent codes, we randomly sample  $n = 500$  latent codes.

**Out-of-distribution radiance field.** The optimization objective is:

$$\begin{aligned} \mathbf{T}^{O*}, \theta_{D^O}^*, \phi_t^* &= \underset{\mathbf{T}^O, \theta_{D^O}, \phi_t}{\operatorname{argmin}} \mathcal{L}_t^O \\ &= \underset{\mathbf{T}^O, \theta_{D^O}, \phi_t}{\operatorname{argmin}} \sum_{ij} \|(\mathbf{C}_t^O(\mathbf{r}_{ij}) - \mathbf{C}^{GT}(\mathbf{r}_{ij})) \cdot \mathbf{M}_t(\mathbf{r}_{ij})\|_2^2, \end{aligned} \quad (15)$$

where  $\mathbf{T}^O(t_k) \in \mathbb{R}^{32}$  is the aggregated features obtained by projecting 3D coordinate  $t_k$  onto each of the three feature planes via bilinear interpolation, then aggregated via summation [9]. The decoder  $D^O$  is an MLP with weights of  $\theta_{D^O}$ .  $\mathbf{C}^{GT}(\mathbf{r}_{ij})$  is the ground-truth color at pixel  $(i, j)$ .

**Composite rendering.** The goal is

$$\begin{aligned}
 \mathbf{T}^{O*}, \theta_{DO}^*, \phi_t^* &= \operatorname{argmin}_{\mathbf{T}^O, \theta_{DO}, \phi_t} \mathcal{L}_t^C \\
 &= \operatorname{argmin}_{\mathbf{T}^O, \theta_{DO}, \phi_t} \sum_{ij} \|C^C(\mathbf{r}_{ij}) - C^{GT}(\mathbf{r}_{ij})\|_2^2 \\
 &+ \lambda_b \mathcal{L}_b(\mathbf{r}_{ij}) + \sum_{\mathbf{M}_t(ij) \neq 1} \lambda_{spar} \mathcal{L}_{spar} + \mathcal{L}_{LPIPS}(\mathbf{I}_{LR}^C, \mathbf{I}_{LR}),
 \end{aligned} \tag{16}$$

where  $\mathcal{L}_{LPIPS}$  is LPIPS loss [63],  $\mathbf{I}_{LR}^C$  is the composite rendered image at low resolution ( $128 \times 128$ ),  $\mathbf{I}_{LR}$  is the ground truth image also at  $128 \times 128$ .  $\mathcal{L}_{spar}$  is a sparsity loss used to suppress the blending weights for the OOD pixels outside the mask. We use this regularization in case the OOD radiance field dominates, which makes the editing trivial, since we rely on the in-distribution part for the editing.

$$\mathcal{L}_{spar}(\mathbf{r}) = \sum_{k=1}^K \mathcal{L}_1(b(t_k)), \tag{17}$$

weight regularizer  $\mathcal{L}_b$  is adopted from [55], used to penalize the blending weight  $b$  if it is not closer to 0 or 1:

$$\mathcal{L}_b(\mathbf{r}) = \sum_{k=1}^K H_b(b(t_k)), \tag{18}$$

where  $H_b(x) = -(x \log(x) + (1-x) \log(x))$  is binary entropy. The reason behind Eqn. 18 is that objects cannot co-occupy *the same spatial location*. The entropy loss facilitates a cleaner decomposition to be either an in-distribution object (*i.e.*  $b \rightarrow 0$ ) or an out-of-distribution object (*i.e.*  $b \rightarrow 1$ ).

In practice, we optimize for Eqn. 14 only. We then jointly optimize for Eqn. 15 and Eqn. 16.

## B. Additional results for Semi-Supervised method

We compare our unsupervised framework and our semi-supervised framework.

**Hyperparameters.** We use the Adam optimizer [30] for all the experiments. For in-distribution inversion, we optimize for 200 epochs with a learning rate of  $1 \times 10^{-3}$ , the weight of latent variation loss  $\lambda_{\Delta} = 1 \times 10^{-3}$ . For the out-of-distribution and composite rendering, we run the optimization for 200 to 300 epochs depending on the video length with a learning rate of  $5 \times 10^{-3}$ , the weight of blending weight regularizer  $\lambda_b = 1$ , and the weight of sparsity loss  $\lambda_{spar} = 3$ . For the SR module, we fine-tune the module for 100 epochs with a learning rate of  $1 \times 10^{-3}$ .

**Reconstruction.** Compared to the semi-supervised method, our unsupervised method performs slightly worse.

This is because the semi-supervised method works with segmentation masks, which is easier to split a frame into in-distribution and out-of-distribution parts.

Table 5. Quantitative comparison for reconstruction quality.

Metrics	LPIPS↓	$\mathcal{L}_2$ ↓	SSIM↑	PSNR↑	ID similarity↑
Ours (semi-supervised)	<b>0.1981</b>	<b>0.0150</b>	<b>0.7722</b>	<b>19.6985</b>	<b>0.9831</b>
Ours (unsupervised)	<u>0.2237</u>	<u>0.0339</u>	<u>0.7052</u>	<u>16.0287</u>	<u>0.9758</u>
PTI [43]	0.3144	0.0504	0.6320	13.4483	0.9658
IDE-3D [48]	0.4999	0.1172	0.4512	9.5852	0.8251
$\mathcal{W}^+$	0.3380	0.0383	0.6557	14.7486	0.9154
$\mathcal{W}$	0.4030	0.0618	0.5787	12.4769	0.8652

**Editing.** We report the evaluation of editing in Table 6. Similar to the reconstruction, the semi-supervised method preserves better editability. This is because, with masks to separate the in-distribution and out-of-distribution radiance fields, we make the in-distribution part (generated by the latent code) lie closer to the latent space of the pre-trained EG3D. This enables better editability.

Table 6. Quantitative comparison for identity preservation after editing. Higher numbers indicate better identity preservation.

	“eyeglasses”	“surprised”	“younger”	“smile”	“Elsa”
Ours (semi-supervised)	<b>0.9368</b>	<b>0.9816</b>	<b>0.9457</b>	<b>0.9556</b>	0.8610
Ours (unsupervised)	<u>0.9158</u>	<u>0.9360</u>	<u>0.9347</u>	<u>0.9094</u>	<u>0.8927</u>
PTI	0.9049	0.9357	0.9319	<u>0.9336</u>	0.7945
IDE-3D	0.8767	0.9481	0.8551	0.8662	0.7871
$\mathcal{W}^+$	0.8971	0.9249	0.9290	0.9170	0.7968
$\mathcal{W}$	0.8793	0.9537	0.9068	0.9208	0.8113

**Speed.** We also report the speed of different approaches in Table 7. The semi-supervised method is slower than the unsupervised method due to an additional loss function (Eqn. 15).

Table 7. Speed for different baselines on 200 frames.

PTI [43]	IDE-3D [48]	Ours (unsupervised)	Ours (semi-supervised)
2.18h	95s	3.17h	3.54h

**Conclusion.** Compared to the semi-supervised method, our proposed unsupervised method

- works automatically without humans in the loop,
- converges faster than the semi-supervised method,
- but performs slightly worse than the semi-supervised method.

This enables different application scenarios given our proposed framework. If we have the segmentation masks, either from off-the-shelf algorithms or manual labels, then we can use them to achieve better performance. However, if we pursue a fully automatic approach, then our unsupervised framework can be used.